Noname manuscript No.
(will be inserted by the editor)

Near-Surface Vertical Flux Divergence in the Stable Boundary Layer

L. Mahrt · Christoph K. Thomas · Andrey A. Grachev · P. Ola G. Persson

Received: DD Month YEAR / Accepted: DD Month YEAR

Abstract Flow in the stable boundary layer is examined at four contrasting sites with greater upwind surface roughness. The surface heterogeneity is disorganized and in some cases weak as commonly occurs. With low wind speeds, the vertical divergence (or convergence) of the momentum and heat fluxes can be large near the surface in what is normally assumed to be the surface layer where such divergence is neglected. For the two most heterogeneous sites, a shallow "new" boundary layer is captured by the tower observations, analogous to an internal boundary layer but more complex. Above the new boundary

L. Mahrt
NorthWest Research Associates
2171 NW Kari Pl
Corvallis, OR, USA, 97330
E-mail: mahrt@nwra.com

Christoph K. Thomas
Micrometeorology Group
University of Bayreuth
95540 Bayreuth
Germany

Andrey A. Grachev
NOAA Earth System Research Laboratory / Cooperative Institute for Research in Environmental Sciences,
University of Colorado, Boulder, Colorado, USA

P. Ola G. Persson
NOAA Earth System Research Laboratory / Cooperative Institute for Research in Environmental Sciences,
University of Colorado, Boulder, Colorado, USA

layer, the magnitudes of the downward fluxes of heat and momentum increase with height in a transition layer, reach a maximum, and then decrease with height in an overlying regional boundary layer. Similar structure is observed at the site with rolling terrain where the shallow new boundary layer at the surface is identified as cold air drainage generated by the local slope above which the flow undergoes transition to an overlying regional flow. Significant flux divergence near the surface is generated even over an ice floe for low wind speeds in a shallow Ekman layer that forms during the polar night. For higher wind speeds, the magnitude of the downward fluxes decreases gradually with height at all levels as in a traditional boundary layer.

Keywords Internal boundary layer · Nocturnal boundary layer · Roughness change · Stable boundary layer · Vertical flux divergence

1 Introduction

The vertical flux divergence near the surface of the nocturnal boundary layer can be sufficiently large that fluxes measured at standard observational levels do not adequately estimate the surface flux. The surface layer may be confined to a layer below the lowest observational level. Common shallow drainage flows are an example where the fluxes may vary significantly with height even in the lowest few metres. The stress can approximately vanish at the wind-speed maximum of the drainage flow where the speed shear vanishes (Grisogono and Oerlemans, 2001; Nadeau et al., 2013); see also Mahrt et al. (2014).

Fluxes can also vary rapidly with height in flow over an abrupt transition from rougher to smoother surfaces. An internal boundary layer develops that is attached to the downwind smoother surface and is characterized by smaller turbulence intensity compared to upwind locations (Garratt, 1990, 1994). Based on large-eddy simulations (LES), Glendening and Lin (2002) found that the magnitude of the downward momentum flux increases with height immediately downwind of a rough-to-smooth transition in stable conditions. In offshore flow from a rough warm land surface over a smooth cooler sea surface, Skyllingstad et al. (2005) showed a significant increase of the friction velocity (u_*) with height up to 100 m. Pöette et al. (2017) found that downwind of a rough-to-smooth transition in a wind tunnel, the turbulent energy and magnitude of the downward momentum flux both increase with height up to a maximum and then decrease with further increase in height (e.g., their Fig. 7). Their observations include a sequence of transitions where this vertical structure is modified compared to a single transition, but the basic spatial structure remains intact. Details depend on the relative spacing of the transitions.

For flow from smoother to rougher surfaces, the magnitudes of the downward momentum flux over locally rougher surfaces may decrease with height more rapidly than over homogeneous surfaces, as can be inferred from Morse et al. (2002) and Dellwik et al. (2013). The fetch required for development of an equilibrium layer extending to a certain height is greater in stable conditions (Dellwik and Jensen, 2000) and depends on the particular turbulence variable analyzed (Irvine et al., 1997).

Based on Bou-Zeid et al. (2007), a regional boundary layer above the internal boundary layer can be partitioned into a lower region that is horizontally heterogeneous due to memory of the upwind surface variability, and an upper region above the "blending height" where the flow is horizontally homogeneous; see also Schmid and Bünzli (1995). Bou-Zeid et al. (2007) emphasize the difficulty of defining a unique blending height even within a LES setting. In flow from a rough surface to a smoother surface, the magnitude of the downward fluxes of heat and momentum increase with height from the low turbulence intensity in the new boundary layer to the higher turbulence intensity in the regional boundary layer where turbulence is advected from the upwind rougher surface. Actual surfaces are commonly characterized by complex surface heterogeneity rather than a single discontinuity of surface conditions. These surfaces have been examined much less and are an important part of the present study.

The downward momentum and heat fluxes near the surface may also increase with height due to elevated shear generation of turbulence (Mahrt and Vickers, 2002; Balsley et al., 2006; Sun et al., 2013; Acevedo et al., 2015). The increase of turbulence intensity and magnitude of the downward fluxes with increasing height has been attributed to the generation of turbulence at higher levels where the stratification is less and shear is often maintained by a low-level jet (Conangla and Cuxart, 2006; Banta et al., 2006; Van de Wiel et al., 2010; Kallistratova and Kouznetsov, 2012). Elevated turbulence may be transported downward toward the surface in the form of bursts (Nappo, 1991). Based partly on radon measurements at different heights, Williams et al. (2013) constructed a classification of very stable boundary layers, which includes the top-down case where the turbulence is generated primarily at higher levels. Mortarini et al. (2017) show examples of complex profiles of the stress associated with larger-scale surface heterogeneity, submeso motions, and a low-level jet.

Even over homogeneous flat surfaces, the vertical structure of the fluxes in very stable conditions is sometimes challenging to measure because the boundary-layer depth can be less than 10 m, as found by Smedman (1988), Grachev et al. (2005) and others. With the usual guidelines, surface-layer similarity theory is valid only in the lower 10% of the boundary layer so that measurements of the surface fluxes would be required below 1 m. Because similarity theory is potentially valid only above the roughness sublayer of the vegetation, the surface layer can be potentially "squeezed" out of existence. These boundary layers can still be "traditional" in that the main source of turbulence is due to the surface roughness and the turbulence decreases monotonically with height, as in Fig. 1 of Banta et al. (2006). In addition to difficulties due to the thinness of the boundary layer, Poulos and Burns (2003) found maximum flux divergence at the surface. For observational levels above the shallow surface layer, local similarity theory may still describe the local flux-gradient relationship (Grachev et al., 2013). However, over complex surface heterogeneity, local similarity theory cannot be used to predict the surface fluxes based on the traditional local flux-gradient relationships and generalizations are required (Grachev et al., 2018).

Our study investigates the momentum and heat fluxes near the surface at three contrasting sites with different degrees of complex heterogeneity and a fourth site with a relatively homogeneous surface. The sites are described in Sect. 2.1, and the dependence of the vertical structure on wind speed and stratification is discussed in Sect. 3. The profile characteristics of momentum and heat fluxes are analyzed for different subclasses of the flow in Sects. 4 – 5.

2 Measurements and Analysis

2.1 Field programs

Sonic anemometer measurements were collected in the North Park Basin, Colorado, USA, during winter 2002–2003 in the Fluxes Over a Snow Surface II field program (FLOSSII, $http://www.eol.ucar.edu/isf/projects/FLOSSII/$). See Table 1 for instrument information. On average, the basin floor is about 30 km wide with basin sidewalls of 1,000 m over a horizontal width of about 7 km. The basin is approximately 50 km from south to north. The surface at the tower base consists of matted grass, sometimes with a shallow snow cover;

the roughness length for this site is small, less than 1 mm with snow cover. Scattered short brush begins 100–200 m upwind of the tower with respect to the prevailing southerly flow. Some scatter brush occur upwind for all wind directions. The distribution of the brush is somewhat disorganized with a typical height on the order of 0.1 m. A map of the complex spatial distribution of the brush is provided in Mahrt and Vickers (2005). As a measure of the stratification, $\delta\theta$ is computed as the vertical difference in potential temperature between 1.0 and 5.0 m. The FLOSSII dataset is the longest dataset of the three mid-latitude sites (4 months) and has the tallest tower (30 m) and is used as the default dataset.

The Shallow Cold Pool (SCP) Experiment was conducted over semi-arid grasslands in north-east Colorado, USA, from 1 October to 1 December 2012 ($https://www.eol.ucar.edu/field\_projects/scp$). The main valley is relatively small, roughly 12 m deep and 270 m across with valley side slopes generally $< 6°$. Widely scattered short brush grows upwind 100–200 m from the tower with respect to the prevailing wind direction of west-north-west to north-west. We analyze sonic anemometer measurements taken from the main tower (Table 1) with $\delta\theta$ computed between the heights of 1.0 m and 5.0 m; see Mahrt and Thomas (2016) for more information on this site. The estimation of the roughness length is uncertain because of frequent distortion of the wind profile by the local topography.

A 12-m tall eddy-flux tower was deployed at the Botany and Plant Pathology (BPP) Farm of Oregon State University, USA (Thomas et al., 2012). We analyze observations from late August until mid-October 2011 (Table 1). Regardless of wind direction, the upwind roughness length is greater than that at the grass-covered tower location due to upwind orchards, row crops and hedges and a nearby building (see vegetation map in Zeeman et al. (2015)). The effective roughness length is wind-direction dependent but always greater than about 25 mm and presumably influenced by the upwind vegetation. The airflow generally passes over a sequence of roughness changes before arriving at the tower site. The quantity $\delta\theta$ is computed by interpolating the 12 levels of Omega TMTSS-020G thermocouple data to the heights 1.0 and 5 m. The thermocouple levels are at 0.05, 0.1, 0.2, 0.4, 0.8, 1.5, 3, 4, 6, 8, 10 and 12 m.

The Surface Heat Budget of the Arctic Ocean Experiment (SHEBA) tower flux measurements (Persson et al., 2002; Grachev et al., 2005) were made from October 1997 to October 1998 on a multi-year ice floe drifting in the Beaufort and Chukchi Seas. The measurements analyzed in our study are listed in Table 1. The SHEBA site was located a few hundred kilometers from land on Arctic pack ice, which had no large-scale slopes. The surface is generally smooth snow-covered ice, though patches of ice rubble up to 3 m in height exist in most directions at distances of several hundred metres to a few kilometres. The roughness lengths increase by a factor of two with the height of the observations over the depth of the tower, indicating that a footprint higher on the tower includes some of the rougher ice at greater distances (Persson et al., 2002). Based on fluxes closest to the surface, the roughness lengths are small (typically 5×10^{-4} m), indicating a relatively smooth surface. Data contaminated by huts and the ship in the southerly and south-westerly direction comprise about 10% of the data and have been eliminated; the remaining data are predominantly from the unobstructed and dominant north-easterly and north-westerly wind directions.

During the polar night at the SHEBA site (early November through early February), stable conditions are long lasting and can reach quasi-stationary states compared to those in the midlatitudes. The boundary-layer stability is primarily modulated by synoptic and mesoscale disturbances and the clouds they produce (Persson et al., 2017) with time scales of 12 h to 5 days. The summer period has been removed because the very few cases of stably stratified flow in this season are associated with warm-air advection from ice-free areas and compromise the assumption of relatively homogeneous conditions. Because the SHEBA data is much more stationary than the other datasets, we use the fluxes from the high-frequency portion of the 13.65-min covariance spectra averaged for 54 min, as described by Grachev et al. (2005). This high-frequency portion represents turbulent motions with time scales of at most 2–3 min. $\delta\theta$ is computed between the 2.2-m and 8.9-m levels. To compare with the other three sites where $\delta\theta$ is estimated over a 4-m layer, $\delta\theta$ at the SHEBA site is multiplied by 4 m/6.7 m. This does not correct for the typical decrease of the temperature gradient with height.

For the three mid-latitude datasets, we analyze only measurements between 2100 and 0600 LST (local standard time) to exclude daytime and transition periods. No conditions were imposed on time of day for the SHEBA measurements, but instead measurements are included only when $\delta\theta > 0.1$ K, which excludes neutral conditions and conditions where the stable stratification might be too small to accurately measure. This condition on the stratification eliminates some of the cloudy periods during the polar night as longwave radiation from clouds sometimes produces neutral stratification (Persson et al., 2017). Also, only winter and spring data are used. For the retained SHEBA data, 83% occurred during the polar night with little insolation while 17% represent nocturnal stable boundary layers during March and April when a significant diurnal cycle develops (Persson et al., 2002).

2.2 Challenges Computing Momentum Fluxes for Very Stable Conditions

Estimation of the momentum flux divergence is more sensitive to errors than the momentum flux itself. The problem is particularly difficult for low wind speeds and stable stratification. For wind speeds < 2 m s^{-1}, about 20% of the wind directions correspond to flow through the tower, depending on the site and the definition of "through the tower." Data with flow through the tower were not eliminated at the FLOSSII, SCP and BPP sites because such elimination would have led to highly segmented time series for low wind speeds.

Loss of momentum flux due to path-length averaging is a concern with very stable conditions where some of the turbulent transport might be on scales that are not adequately resolved because of sonic path-length averaging. The heat-flux cospectra in FLOSSII indicates that the heat flux at 2 m is fully resolved (Mahrt and Vickers, 2006) such that the variation of the flux between 2 and 30 m is probably not affected by path-length averaging. The method of Horst and Oncley (2006) indicated that the heat flux was fully resolved for 1 m and above at the SCP site. The method of Moore (1986) had been applied to the BPP measurements, and the impact of path-length averaging appears to be small compared to the rapid increases of flux magnitude with height at the BPP site.

Unfortunately, the above methods rely on cospectral similarity theory and our cospectra for very stable conditions include cases where an inertial subrange is not evident as shown by Grachev et al. (2013) for the SHEBA measurements. The path-length averaging flux loss should be greatest at the surface where the transporting eddies are smallest and thus acts to increase the flux magnitude with height. Yet the flux magnitude for low wind speeds at the FLOSSII and SCP sites tends to decrease with increasing height closest to the surface and increase with height only at higher levels (Sect. 5). This circumstantial information implies that path-length averaging is not a serious problem.

The choice of averaging time that determines the largest scales included in the flux computation becomes uncertain for very stable conditions where turbulent and non-turbulent motions may overlap in scale. The averaging times for the FLOSSII, SCP and BPP sites are chosen to be 1 min as a compromise between minimizing the impact of the non-turbulent motions on the computed fluctuations and minimizing the loss of turbulent flux for higher wind speeds. The optimum averaging length may be a strong function of stability. Fortunately, the results of this study based on composited (bin-averaged) quantities are not particularly sensitive to the choice of averaging time for these datasets, at least within the range of 30 s to 300 s.

A more detailed analysis of the FLOSSII measurements indicated that the momentum flux depends significantly on the choice of the coordinate alignment rotation ("tilt" rotation) for very low wind speeds < 0.5 m s^{-1}. With larger stratification, the transporting motions are generally flatter, causing smaller attack angle with respect to the anemometer, which in turn increases the impact of misalignment of the sonic anemometer. Coordinate alignment attempts to reduce the misalignment of the sonic anemometer with respect to the surface and also reduces the impact flow distortion depending on the rotation method and type of sonic anemometer. Misalignment with respect to sloped terrain in the footprint of the flux measurement depends on wind direction, wind speed and stability and sometimes includes the impact of microscale flow separation on the attack angle of the flow (Stiperski and Rotach, 2016).

The datasets varied in terms of cross-wind corrections (Liu, 2001) which were found to be quite small. The datasets also varied in terms of corrections for instrument-induced flow distortion (Horst et al., 2015) or in terms of wind-tunnel calibration. For low wind speeds and strong stratification, we believe these errors are small compared to the difficulties of correcting for sonic misalignment and potentially significant flux loss to path-length averaging. In spite of the above efforts to assess flux errors, we cannot categorically assume that instrumental problems do not significantly influence the estimated stress

Table 1 Site description. Total months of data, sonic-anemometer model, tower levels (m), sampling rate (SR in samples per second) and tilt-rotation method (TM) where PF = planar fit (Wilczak et al., 2001), DR = double rotation (Grachev et al., 2005) and DPF = directionally dependence planar fit (Acevedo and Mahrt, 2010).

site	months	sonic	tower levels	SR	TM
FLOSSII	4	Campbell CSAT3	1 2 5 10 15 20 30	40	DPF
SCP	2	Campbell CSAT3	0.5 1 2 3 4 5 10 15 20	20	PF
BPP	2	Metek USA-1	0.8 3	10	DPF
BPP	2	R. M. Young 81000 VRE	7.5 12	10	DPF
SHEBA	7	ATI	2.2 3.2 5.1 8.9 13.8	20	DR

divergence, although it is not obvious how such errors would lead to systematic variation of the flux with height.

2.3 Time Averaging

Our analysis approach is described in Mahrt and Thomas (2016) with the flow is partitioned as

$$\phi = \phi' + \overline{\phi}, \quad (1)$$

where the overbar designates a time average over a window of width τ, ϕ' is the deviation from such an average, ϕ is potential temperature or one of the velocity components, fluxes are computed as $\overline{w'\phi'}$ where w' is the perturbation vertical velocity, and the wind speed is determined as

$$V \equiv \sqrt{\overline{u}^2 + \overline{v}^2}. \quad (2)$$

2.4 Averaging Over Intervals

Because we use small averaging windows to filter out non-turbulent motions and reduce flux bias, averages for individual windows are characterized by large uncertainty due to random-like variations. As a result, we bin-average (composite) the window averages separately for different intervals of some variable such as height above ground or the wind speed. Narrow intervals (bins) are chosen to construct a semi-continuous dependence of the turbulence on the forcing variable. Broader intervals are chosen to construct classes such as the low wind class $V < 2$ m s^{-1} and the high wind class $V > 6$ m s^{-1}. Either type of compositing is symbolized by square brackets such as $[\overline{\phi}]$.

Non-stationarity and variation of vertical structure of the flux between nights prevent interpretation of the composited variables (bin averages) in terms of an ensemble average and also preclude clear interpretation of the standard error. The standard errors are generally very small, often not even visible if plotted. These small magnitudes result from the large number of 1-min records. However, because of the lack of independence of 1-min records with typical non-stationarity, the standard error can substantially underestimate the actual flux uncertainty (Mahrt and Thomas, 2016).

2.5 Different Calculations of the Momentum Flux

The method of computing the momentum flux becomes important with low wind speeds. Unless otherwise noted, the x-direction refers to the along-wind coordinate at each level such that the along-wind momentum flux is $\overline{w'u'}$ and the crosswind flux is $\overline{w'v'}$. The total momentum flux in this *height-dependent rotated coordinate system* is written as

$$\overline{w'\boldsymbol{V}'} \equiv \overline{w'u'}\ \boldsymbol{i} + \overline{w'v'}\ \boldsymbol{j}, \tag{3}$$

where $\boldsymbol{i}$ and $\boldsymbol{j}$ are unit vectors in the along-wind x and crosswind y directions, respectively. The flux components are composited over all of the values within a given bin or class to obtain $[\overline{w'u'}]$ and $[\overline{w'v'}]$, and we define the shorthand notation for the magnitude of the composited momentum flux as

$$[\overline{w'\boldsymbol{V}'}] \equiv ([\overline{w'u'}]^2 + [\overline{w'v'}]^2)^{0.5}. \tag{4}$$

Here, the square brackets on the left-hand side imply that the flux components are composited first.

When analyzing data with wind-directional shear, a more meaningful flux divergence might be computed in a coordinate system that is fixed with height, sometimes based on the direction of the surface wind (surface-based rotation) where

$$\overline{w'\boldsymbol{V}'_{sfc}} \equiv \overline{w'u'_{sfc}}\ \boldsymbol{i} + \overline{w'v'_{sfc}}\ \boldsymbol{j}. \tag{5}$$

However, with small wind speed and significant stratification and resulting partial decoupling in the vertical, the direction of the wind vector at higher levels can become more chaotic in a surface-based coordinate system. In addition, the wind vector can systematically shift with height away from the surface wind direction. As a result of compositing over flux components of varying sign, $[\overline{w'\boldsymbol{V}'}_{sfc}]$ decreases rapidly with height in the surface-based coordinate system (black, Fig. 1a) in contrast to $[\overline{w'\boldsymbol{V}'}]$ in the locally rotated coordinate system (red line, Fig. 1a), which increases slowly with height.

Comparing $[\overline{w'u'}]$ (red dashed) with $[\overline{w'\boldsymbol{V}'}]$ (red) indicates that the composited cross-wind momentum flux is small for the FLOSSII site although it can be large for individual profiles. Using 5-min averaging instead of 1-min averaging has little effect on the composited wind and stress profiles (compare cyan and red lines, Fig. 1a). The differences between the various profiles become significantly smaller with higher wind speeds (Fig. 1b).

Compositing the friction velocity

$$u_* \equiv (\overline{w'u'}^2 + \overline{w'v'}^2)^{0.25} \tag{6}$$

to obtain $[u_*]$ must be interpreted with caution. The contributions of the deviations of the flux components from their composited values contribute significantly to $[u_*]$ but do not contribute to $[\overline{w'V'}]$. The contribution of random-like variations of $\overline{w'V'}$ can be interpreted as bias in the calculation of $[u_*]$ if $[u_*]$ is interpreted as a measure of the systematic momentum flux. To construct an exercise illustrating this process, we partition each flux component into the

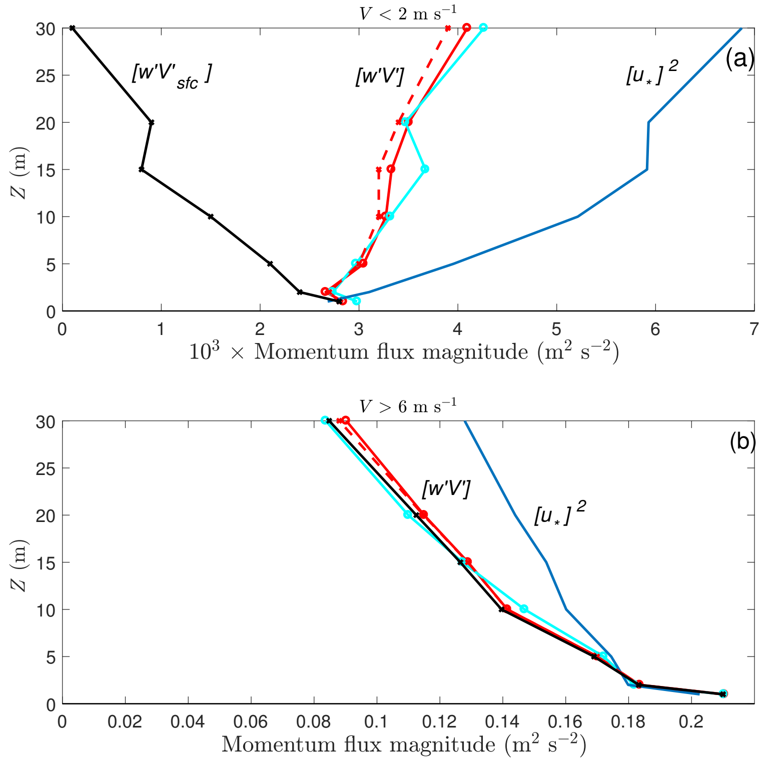

Fig. 1 Height dependence of the composited (bin-averaged) momentum flux at the FLOSSII site for a) $V < 2$ m s^{-1} and b) $V > 6$ m s^{-1}. Plotted are the composited stress magnitudes based on Eq. 4 with the height-dependent rotated coordinate system (solid red, $[\overline{w'\boldsymbol{V}'}]$), with the height-dependent rotated coordinate system but with 5-min window averages (cyan), with the along-wind flux component only (red dashed, $[\overline{w'u'}]$), and with the coordinate system rotated into the surface wind direction ($[\overline{w'\boldsymbol{V}'}_{sfc}]$, black line). The blue line is the scalar composite $[u_*]^2$.

composited momentum flux and a deviation from this value. Then each value of u_* can be written as

$$u_* = (([\overline{w'u'}] + \hat{\overline{w'u'}})^2 + ([\overline{w'v'}] + \hat{\overline{w'v'}})^2)^{0.25}, \qquad (7)$$

where the hat symbol above the overbar designates deviations from the composited value that include random variations. To avoid the need for a complex series expansion, we raise Eq. 7 to the fourth power to obtain

$$u_*^4 = [\overline{w'u'}]^2 + 2[\overline{w'u'}]\hat{\overline{w'u'}} + \hat{\overline{w'u'}}^2 + [\overline{w'v'}]^2 + 2[\overline{w'v'}]\hat{\overline{w'v'}} + \hat{\overline{w'v'}}^2. \qquad (8)$$

Compositing each side and noting that $[[\overline{w'u'}]\widehat{\overline{w'u'}}]$ and $[[\overline{w'v'}]\widehat{\overline{w'v'}}]= 0$,

$$[u_*^4] = [\overline{w'u'}]^2 + [\overline{w'v'}]^2 + ([\widehat{\overline{w'u'}}]^2 + [\widehat{\overline{w'v'}}]^2). \tag{9}$$

The terms $[\widehat{\overline{w'u'}}]^2$ and $[\widehat{\overline{w'v'}}]^2$ augment $[u_*^4]$ but not $[\overline{w'V'}]$ and $[\overline{w'u'}]$; $[u_*]$ increases monotonically with increasing $[u_*^4]^{1/4}$ in a way that depends on the frequency distribution of $[u_*]$ not pursued here.

The augmentation of $[u_*]$ above $[\overline{w'V'}]$ and $[\overline{w'u'}]$ for the current data is quantified in Fig. 1 (compare blue line with red solid and dashed lines). If the square brackets represented a true ensemble average, the contributions of $[\widehat{\overline{w'u'}}]^2$ and $[\widehat{\overline{w'v'}}]^2$ could be viewed as inadvertent conversion of random error to systematic momentum flux. Although u_* represents the magnitude of the momentum flux for an individual averaging window, $[u_*]$ cannot be thought of as a pure measure of the systematic momentum flux. Instead, the composited friction velocity, $[u_*]$, provides a measure of the intensity of the turbulence that is based on the momentum flux. For the FLOSSII dataset, σ_w and u_* are linearly correlated with a ratio of about 1.4, within the range for stable conditions summarized in Garratt (1994) and also in general agreement with Fig. 4 in Pahlow et al. (2001) and Fig. 6 in Basu et al. (2006). However, in our datasets, σ_w is more likely to increase with height near the surface than u_* (not shown) noting that σ_w unavoidably includes some influence of non-turbulent motions. On the other hand, Acevedo et al. (2009) advises against using u_* as a scaling variable for low wind conditions because of its sensitivity to mesoscale variability and recommends use of σ_w instead. For our measurements, the vertical profile of u_* lies between the profiles of σ_w and the along-wind momentum flux $[\overline{w'u'}]$.

2.6 Vertical Structure

Section 3 examines the behaviour of vertical structure based on the traditional scaling variable u_* which is used as a measure of the intensity of the turbulence based on the momentum flux. To avoid fitting complex individual profiles that occur in very stable conditions, we compute the vertical difference based on simple finite differencing defined as

$$\delta_z u_* \equiv u_*(z_2) - u_*(z_1), \tag{10}$$

where the operator δ_z takes the difference of u_* between the two levels. We evaluate Eq. 10 as close to the surface as possible yet include sufficient layer thickness to control the impact of observational errors on the computed vertical differences. As a compromise, the heights z_1 and z_2 are chosen to be the 1- and 5-m levels for the FLOSSII and SCP sites, the 0.8- and 7.5-m levels for the BPP site and the 2- and 8-m levels for the SHEBA site. To reduce the effect of the larger vertical interval, we multiply the differences by 0.6 for the BPP site and 0.67 for the SHEBA site.

Section 4 examines the vertical structure of the along-wind momentum flux $[\overline{w'u'}]$ to identify the behaviour of the systematic part of the momentum flux. Because the crosswind momentum flux is of variable sign, the contribution of crosswind momentum flux to the composited profiles is generally small except for the SCP data where shallow drainage flows induce significant directional shear.

3 Dependence of $\boldsymbol{\delta_z u_*}$ on $\boldsymbol{V}$ and $\boldsymbol{\delta\theta}$

3.1 Joint Distribution

We composite the distribution of $\delta_z u_*$ with respect to joint intervals of $\delta_z\theta$ and V at the FLOSSII site (Fig. 2); the advantages of joint distributions

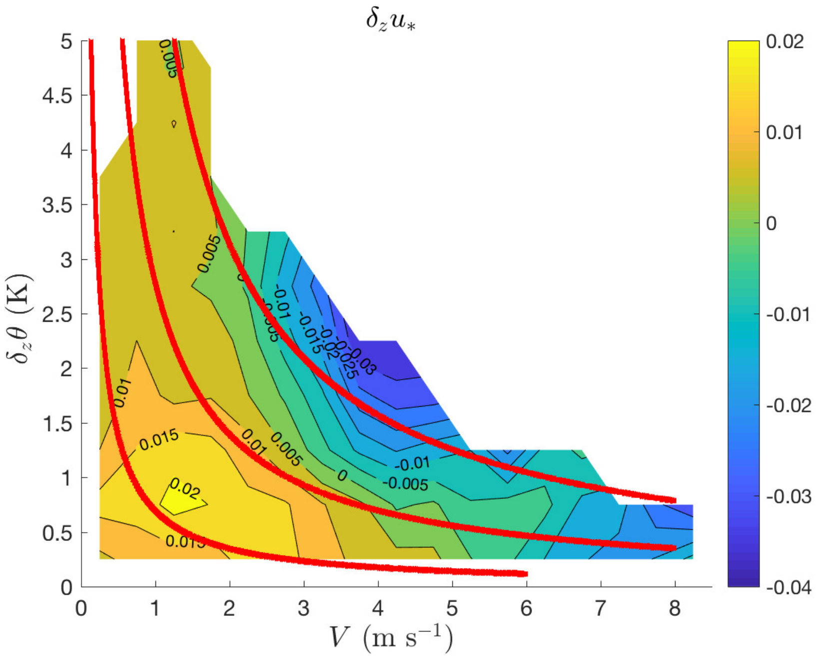

Fig. 2 Dependence of $[\delta_z u_*]$ on V and $\delta\theta$ for the FLOSSII site where $[\delta_z u_*]$ represents compositing jointly over intervals of V and $\delta\theta$. Upper left corresponds to more stable conditions, and the lower right corresponds to near-neutral conditions. Red lines correspond to $V_{\delta\theta} = 0.05$, 0.1 and 0.15 m s^{-1} (Eq. 13).

are discussed in Williams et al. (2013). On average, $\delta_z u_* > 0$ for small V, particularly for small $\delta\theta$. Advection of larger turbulence intensity from the rougher brush upwind from the site (Sect. 2.1) over the less turbulent air above the grass surface probably contributes significantly to the increase of u_* with height ($[\delta_z u_*] > 0$), discussed further in terms of the along-wind momentum flux in Sect. 4.

$[\delta_z u_*]$ is < 0 with larger V at the FLOSSII site (Fig. 2). Decreasing u_* with decreasing height is characteristic of traditional boundary layers. For a given large magnitude of V, the magnitude of $[\delta_z u_*]$ tends to increase with increasing $\delta_z\theta$. Larger $\delta\theta$ generally leads to smaller boundary-layer depth for a given magnitude of V such as implied by the usual decrease of boundary-layer depth with increasing bulk Richardson number. This argument assumes that

$\delta_z u_*$ is proportional to $(u_*)_{sfc}/h$ where h is the stability-dependent boundary-layer depth.

The joint distribution of $\delta_z u_*$ for the SCP site (not shown) is similar to that at the FLOSSII site in spite of the influence of the down-valley drainage flow at the SCP site. However, the joint distribution for the heterogeneous BPP site is less organized beyond a general increase of positive $\delta_z u_*$ with increasing V, in contrast to the FLOSSII and SCP sites, presumably due to an increase of advection of turbulence from the rougher surface immediately upwind from the BPP site (Sect. 2.1). The wind speed is generally confined to small magnitudes at the BPP site, corresponding to a small subdomain of Fig. 2. The joint distribution for the SHEBA site, which includes predominantly small stratification, is less organized. The turbulence and δu_* are smaller at the SHEBA site compared to the other sites (Sect. 4) partly because of the very small roughness length of the snow-covered ice.

3.2 Stability-Dependent Velocity Scales

We now consider two stability-dependent velocity scales based on the mean flow that might better predict $\delta_z u_*$ than predicted by V alone. For the first velocity scale, we begin with the bulk Richardson number

$$Rb \equiv \frac{gz\delta\theta}{\Theta V^2}, \qquad (11)$$

where g is the acceleration due to gravity and z is the height of the wind-speed measurement above the ground (Sect. 2.1). A stability-dependent velocity scale can be formulated from these variables as

$$V_F \equiv C_F V / \sqrt{\frac{\delta\theta}{\Theta}}, \qquad (12)$$

so that V_F is proportional to the inverse square root of the bulk Richardson number but has units of wind speed and thus formally allows a dimensionally consistent examination of the variation of $[\delta_z u_*]$. The parameter C_F is chosen to be 0.04 in order that V_F has roughly the same range as V to facilitate comparison; $[V_F]$ does not better explain the variation of $[\delta_z u_*]$ than does $[V]$ (compare Fig. 3b with Fig. 3a). This result implies that the stability based on the bulk Richardson number does not systematically describe the variation of $[\delta_z u_*]$. Evidently, stability is not the greatest influence on $[\delta_z u_*]$.

The joint distribution (Fig. 2) motivates an alternative stability-dependent velocity of the form

$$V_{\delta\theta} \equiv C_{\delta\theta} V \sqrt{\frac{\delta\theta}{\Theta}}. \tag{13}$$

The coefficient $C_{\delta\theta}$ is chosen to be 300 in order that $V_{\delta\theta}$ has roughly the same range as V. $[\delta_z u_*]$ varies more systematically with $[V_{\delta\theta}]$ (Fig. 3c) than with $[V]$ or $[V_F]$ with the possible exception of the very complex BBP site. In addition, $[\delta_z u_*]$ for all four sites decreases with increasing $[V_{\delta\theta}]$ whereas $[\delta_z u_*]$ may increase or decrease with increasing $[V]$ or increasing $[V_F]$. Positive $[\delta_z u_*]$, where the turbulence increases with height, occurs for small $[V_{\delta\theta}]$ for all of the sites. For a given magnitude of V, $\delta_z u_*$ is more likely to be positive with small $\delta\theta$ (smaller $V_{\delta\theta}$). With larger $\delta\theta$, a shallow traditional boundary layer can develop near the surface (Sect. 4), and $\delta_z u_*$ more likely becomes negative.

However, $[\delta_z u_*]$ at the very heterogeneous BPP site is more sensitive to $[V]$ than to $[V_{\delta\theta}]$. In addition, use of $V_{\delta\theta}$ did not categorically decrease the within-bin standard deviations compared to use of V or V_F. Although $V_{\delta\theta}$ generally better explains the variation of the stress divergence at a given site, compared to V, progress toward a more universal relationship requires other information such as surface roughness, heterogeneity and advection. Such a relationship is beyond the scope of this investigation.

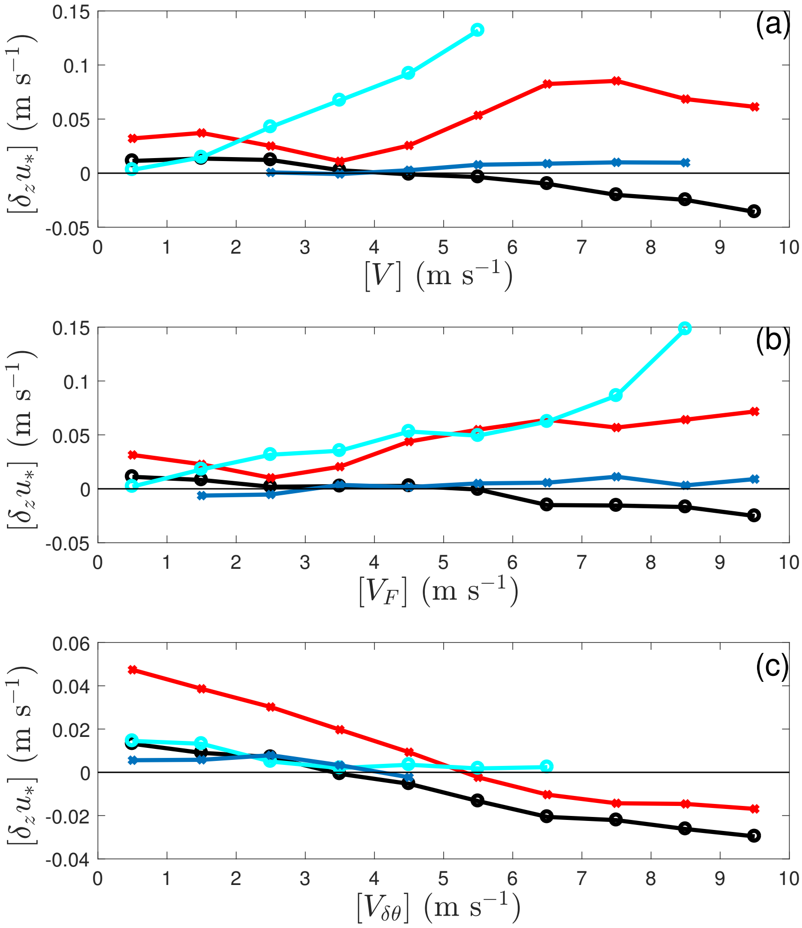

Fig. 3 Dependence of $[\delta_z u_*]$ on the velocity scales for the FLOSSII site (black), the SCP site (red), the BPP site (cyan) and the SHEBA site (blue) for a) $[V]$, b) $[V_F]$ and c) $[V_{\delta\theta}]$. $[V_{\delta\theta}]$ is small for the SHEBA site because of the generally small magnitudes of $\delta\theta$.

4 Vertical Structure for High Wind Speeds

We examine the vertical structure of the fluxes separately for the high-speed class ($V(1\text{ m}) > 6$ m s^{-1}) and the low speed class ($V(1\text{ m}) < 2$ m s^{-1}) as was done in Fig. 1. The low speed class corresponds to the low speed part of

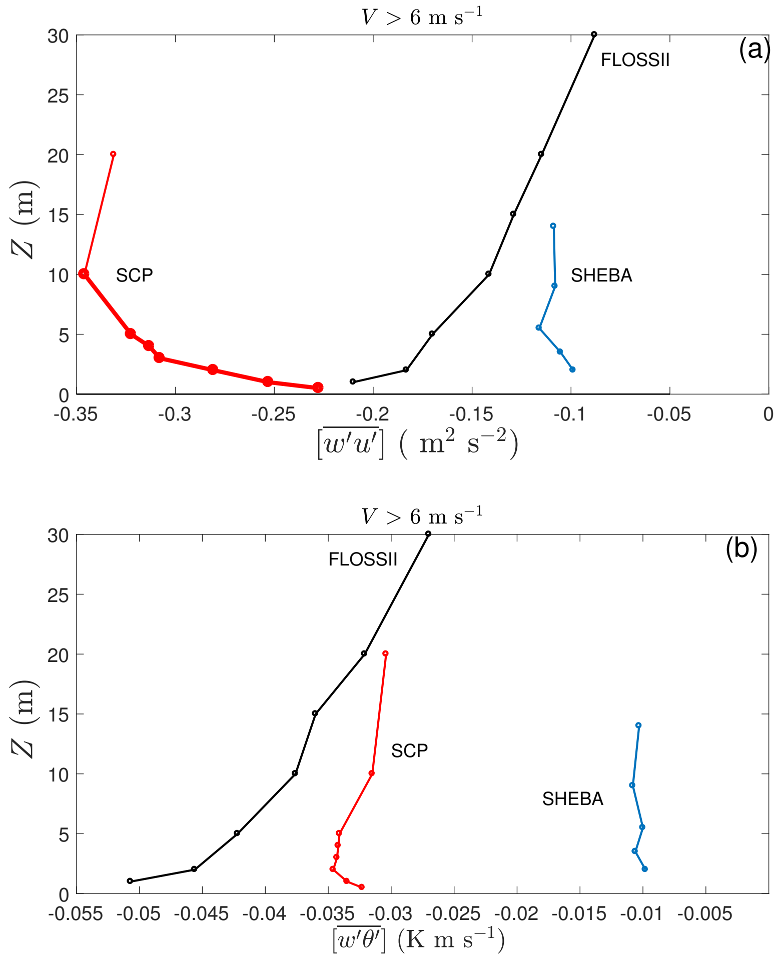

Fig. 4 a) Composited profiles of $[\overline{w'u'}]$ for $V(1\text{ m}) > 6$ m s^{-1} and b) composited $[\overline{w'\theta'}]$, for the FLOSSII (black), SCP (red) and SHEBA (blue) sites. The thicker line identifies a reversed vertical flux gradient (transition layer). The BPP site did not contain sufficient data for the class $V > 6$ m s^{-1}.

the "hockey stick" dependence of u_* on V (Sun et al., 2012), and the high speed class includes only wind speeds substantially higher than the speed at the hockey stick transition.

The low wind (high wind) cases account for 39% (9%) of the FLOSSII records, 61% (2%) of the SCP records, 97% (0%) of the BPP records and 18%

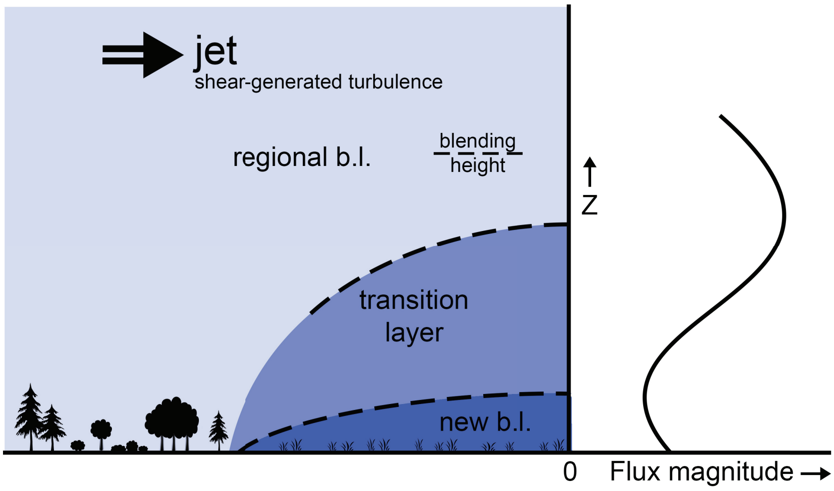

Fig. 5 Plausible example of the new boundary layer at the surface, an overlying transition layer and regional boundary layer, based partly on evidence in the literature (Introduction) and the results of our study. This terminology is more vague compared to that for internal boundary layers (Garratt, 1990) in order to accommodate less-understood flow over complex surface heterogeneity. The blending height partitions the regional boundary layer into a lower layer of horizontal heterogeneity and an upper layer of horizontal homogeneity. In the limit of a single sharp change from rough to smooth surfaces, the new boundary layer and transition layer combine to form the internal boundary layer. In addition, elevated turbulence can be generated by shear instability at higher levels as might occur on the underside of a low-level wind maximum. The diagram on the right illustrates an idealized profile of the magnitude of the downward momentum flux, which reaches a maximum value at the top of the transition layer.

(15%) of the SHEBA records. We now composite the along-wind momentum flux $\overline{w'u'}$ and the heat flux for the high wind class (Fig. 4). The surface flow at the SCP site is influenced by the local slopes and discussed separately in Sect. 5.4.

For $V > 6$ m s^{-1} at the FLOSSII site, the magnitudes of the downward momentum and heat fluxes decrease systematically with height (black, Fig. 4) corresponding to traditional boundary-layer structure. Extrapolation of the momentum flux and heat flux to zero both correspond to a boundary-layer depth of roughly 60 m. For $V > 6$ m s^{-1} at the SCP tower within a shallow valley (red, Fig. 4a), the magnitude of $[\overline{w'u'}]$ increases significantly with height up to 10 m where it reaches a maximum within the vertical resolution of the

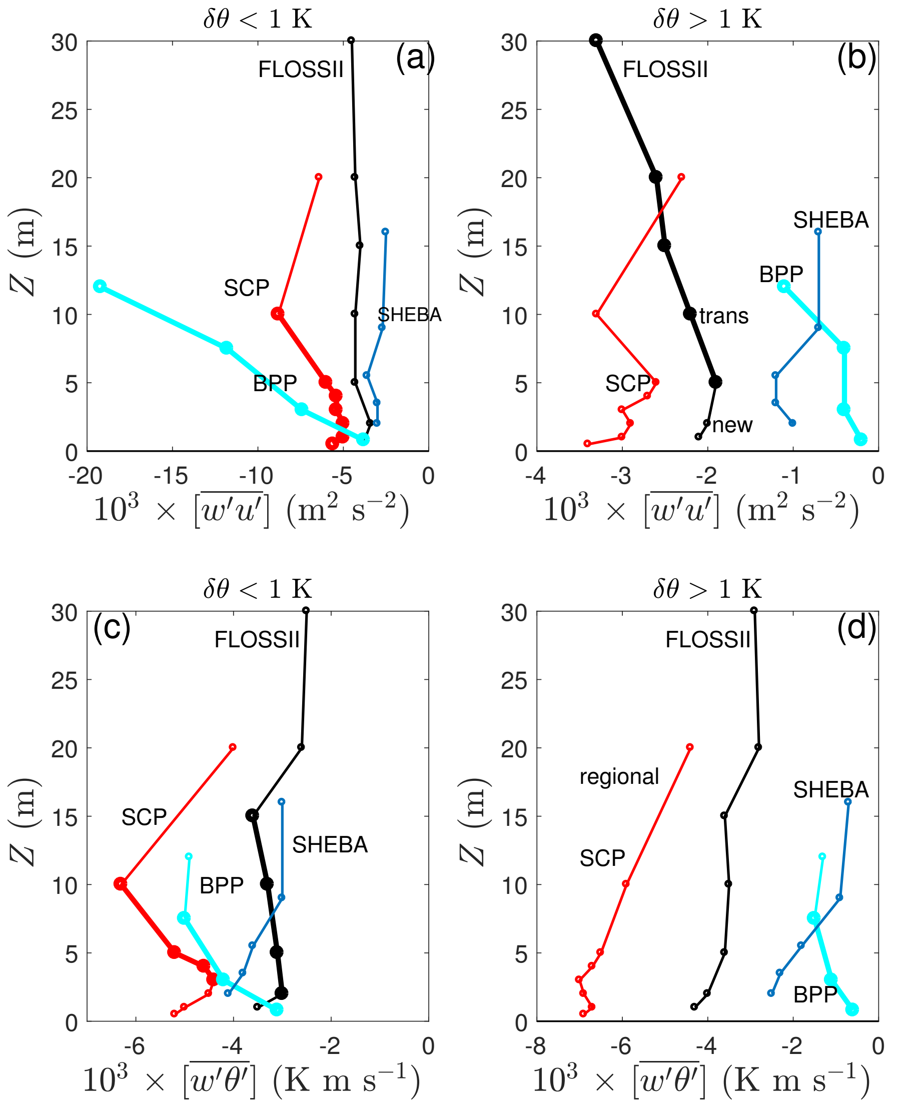

Fig. 6 Profiles of the composited (bin-averaged) stress $[\overline{w'u'}]$ for $V < 2$ m s^{-1} for a) $\delta\theta < 1$ K and b) $\delta\theta > 1$ K and composited $[\overline{w'\theta'}]$ for c) $\delta\theta < 1$ K and d) $\delta\theta > 1$ K. Profiles are shown for the FLOSSII (black), SCP (red), BPP (cyan) and SHEBA (blue) sites. Thicker lines identify reversed vertical flux gradients (transition layer). The labels "new" and "trans" in b) identify examples of the new boundary layer and the transition layer. The label "regional" in d) identifies an example of a regional boundary layer, which is above the tower layer for most of the other profiles.

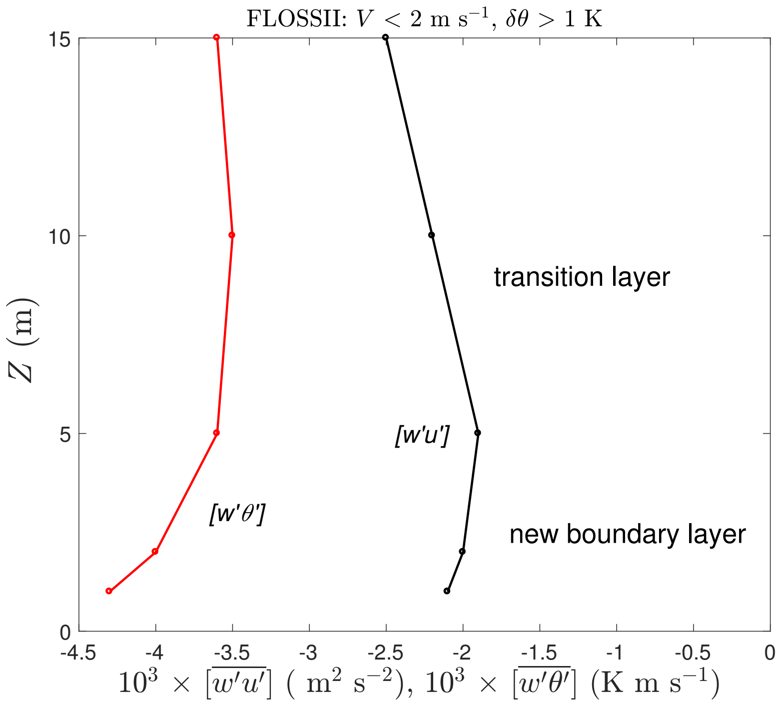

Fig. 7 Composited profiles at the FLOSSII site in the lowest 15 m for $[\overline{w'u'}]$ (black) and $[\overline{w'\theta'}]$ (red) for $V < 2$ m s^{-1} and $\delta\theta > 1$ K. A shallow new boundary layer of roughly 5-m depth, where the flux magnitudes decrease with height, evidently represents at least partial adjustment to the local smaller roughness length.

data. Lee-generated turbulence contributes to this maximum in spite of the small amplitude of the topography, about 12 m depth (Mahrt, 2017). At the homogeneous SHEBA site (blue, Fig. 4), the magnitudes of the downward momentum and heat flux are relatively independent of height with respect to the estimated errors in u_* of 0.015 m s^{-1} (Persson et al., 2002). Generation of turbulence on the underside of low-level jets may maintain the turbulence fluxes at higher levels and prevent significant decrease of the magnitudes of the downward fluxes with height within the tower layer (Persson and Vihma, 2017).

5 Low Wind Speeds

We partition the vertical structure of $[\overline{w'u'}]$ and $[\overline{w'\theta'}]$ for small V into subclasses of smaller and larger $\delta\theta$. We first consider the two sites with complex heterogeneity of surface vegetation. The flow response to such common less organized changes of surface roughness is not understood, but the concept of an internal boundary layer offers guidance. We organize our discussion of low wind speeds over complex heterogeneity in terms of an idealized vertical structure (Fig. 5). We use the purposely vague terms "new boundary layer" and "regional boundary layer" and the transition between these two layers. The flow in the new boundary layer is strongly influenced by the local surface conditions but may not be accommodated by internal boundary-layer theory that was developed for flow past a single discontinuity at the surface. Because we are unable to assess the degree of adjustment of the new boundary layer to the smoother surface, we do not use the term "equilibrium layer" as in internal boundary-layer theory. We sequentially discuss the new boundary layer at the surface, the transition layer and the overlying regional boundary layer at the heterogeneous FLOSSII and BPP sites using the terminology defined in Fig. 5. Because the upwind heterogeneity is complex, the interpretation of the results must be considered somewhat speculative and incomplete.

5.1 New Boundary Layer

For $V < 2$ m s^{-1} and larger stratification ($\delta\theta > 1$ K) at the FLOSSII site, the magnitudes of both the downward momentum and heat flux decrease with height in the lowest 5 m (black, Fig. 6b, d and Fig. 7), suggestive of a shallow new boundary layer that has adjusted, to some degree, to the small local roughness (Sect. 2.1). For small stratification ($\delta\theta < 1$ K), a very shallow new boundary layer might cause the observed decrease of the magnitudes of both the heat and momentum flux between 1 and 2 m (black, Fig. 6a, c) as in a new boundary layer, but this inference is based on only the two lowest levels and must be considered as speculation. The new boundary layer is apparently too shallow to be resolved by the measurements at the BPP site for both stratification categories (cyan, Fig. 6), probably because the upwind greater roughness is close to the tower at the BPP site, only a few tens of metres upwind for the prevailing wind directions.

5.2 Transition Layer

The flux magnitudes increase with height in the transition layer between the new boundary layer and the overlying regional boundary layer (Fig. 6). For $\delta\theta < 1$ K at the FLOSSII site, the magnitude of the downward momentum flux $[\overline{w'u'}]$ increases only very slowly with height up to at least the top of the tower layer (black, Fig. 6a) while the magnitude of the downward heat flux increases more significantly with height but only up to 15 m where it reaches a local maximum (black, Fig. 6c).

For $\delta\theta > 1$ K at the FLOSSII site (black, Fig. 6b and Fig. 7), the magnitude of the downward momentum flux increases more rapidly with height above 5 m compared to the subclass of small stratification. This transition layer extends upward to the top of the tower and presumably above. Because the magnitude of the fluxes cannot increase indefinitely with height, a maximum of the flux magnitude and an overlying regional boundary layer is inferred above the tower layer.

A well-defined transition layer occupies the entire 12-m tower layer for the BPP site for both $\delta\theta$ subclasses (Fig. 6, cyan). The magnitudes of both the downward momentum and heat fluxes increase more rapidly with height at the BPP site (cyan, Fig. 6a,b) compared to that at the FLOSSII site (black) probably because the increase of the height of the upwind vegetation is greater and closer to the tower compared to the scattered upwind brush at the FLOSSII site. The magnitude of the downward heat flux at the BPP site for the low wind class reaches a weak maximum at 8 m for both $\delta\theta$ subclasses (Fig. 6c-d), indicating the bottom of an overlying regional boundary layer. The vertical profile of the heat flux is again characterized by a smaller depth scale than that for the momentum flux.

The different vertical structures for the heat and momentum flux underscore the need for caution in making analogies with internal boundary layers. The heat flux profile is directly influenced by the constraint of the surface energy budget and also by the rapid decrease of the stratification with height for very stable conditions. The momentum flux can be maintained at higher levels due to shear on the underside of low-level jets. All four sites experience low-level jets (not shown). Gravity waves appear to be better organized away from the surface and may also effectively transport momentum.

5.3 Regional Boundary Layer

Maximum magnitudes of the fluxes at the top of the transition layer are explicitly observed for the heat flux at the FLOSSII site for small stratification and to a lesser degree at the BPP site. A maximum in the magnitude of the momentum flux is inferred at some unknown higher level because the flux magnitude cannot increase indefinitely with height. At the FLOSSII site, elevated turbulence can be generated by hills that rise up to 200 m above the tower base, beginning 2–4 km upwind from the tower site with respect to the prevailing wind direction. Higher mountains occur farther upwind. The elevated turbulence is presumably advected over the tower site.

Elevated turbulence was observed from the Wyoming King Air aircraft during FLOSSII (Cardon, 2007). The Wyoming King Air flew nine early morning flights over the FLOSSII tower in February and March of 2003 at 30 m and

60 m above the ground surface. On average, the 30-m aircraft-measured fluxes agreed well with those measured at the top of the tower although the aircraft fluxes were more variable (not shown) probably due to smaller sample size. The magnitude of the momentum flux generally decreased between the 30-m and 60-m levels even with low wind speeds when the flux magnitude tended to increase with height across the tower layer. These observations are consistent with a maximum of the downward momentum flux between 30 and 60 m although the aircraft measurements represent a small amount of data. The magnitude of the aircraft-measured heat fluxes at 60 m were often near zero within suspected observational error. Thus the depth scale for the vertical variation of the heat flux again appears to be smaller than that for the momentum flux. The aircraft soundings showed transient elevated wind maxima but not persistent low-level jets.

5.4 Three-Layer Structure over Gentle Topography

The flow at the SCP tower site for low wind speeds also includes a shallow boundary layer associated with the local surface, a transition layer and a regional boundary layer. However the generation of the flow is different compared to the FLOSSII site. The flow near the surface for low wind speeds at the SCP site is often down the slope of the valley floor. The magnitude of the downward momentum flux at the SCP site decreases with height up to about 5 m for both classes of $\delta\theta$ (red, Fig. 6a-b), defining a shallow new boundary layer at the surface that is responding to the local slope that extends a few hundred metres upwind for the tower. The increase of the magnitude of the downward momentum flux with height between 5 and 10 m is due to generation of turbulence by shear in the vertical transition between the underlying drainage flow and an overlying regional flow (Mahrt et al., 2014), which sometimes leads to significant directional shear.

The magnitudes of the downward heat and momentum fluxes reach a maximum at 10 m for small stratification (red, Fig. 6a, b). For strong stratification, the magnitude of the downward momentum flux reaches a relative maximum at 10 m while the heat flux magnitude reaches a relative maximum at 3 m (red, Fig. 6c, d). These relative maxima define the bottom of the regional boundary layer. Even gentle small-scale topography can lead to complex vertical structure of the flux profile.

5.5 Homogeneous Case

For low wind speeds at the quasi-homogeneous SHEBA site, the magnitudes of the fluxes still decrease significantly with height in the lowest 10 m, more so for the heat flux than for the momentum flux (blue, Fig. 6). Although shallow, this layer can still be referred to as a regional boundary layer although such terminology serves only to make an analogy with the heterogeneous FLOSSII and BPP sites. The shallow boundary layer at the SHEBA site is apparently associated with the very small roughness length and establishment of an Ekman boundary layer where the boundary layer reaches approximate equilibrium during the polar night and the boundary-layer depth becomes constrained by the Earth's rotation (Grachev et al., 2005). The magnitude of the downward momentum flux does not decrease further above 10 m (blue, Fig. 6) possibly because of the influence of background turbulence, turbulence generated by overlying jets, and the impact of cases of deeper boundary layers that are also included in the composite. Grachev et al. (2005) identified several different types of boundary layers that contribute to the composited profiles of our present study. The percentage decrease of the magnitude of the downward heat flux with height is greater compared to that for the momentum flux for both subclasses of $\delta\theta$. As a result, the relatively shallow boundary layer is more clearly revealed by the heat flux profile than the momentum flux profile.

6 Errors in the Surface Flux due to Flux Divergence

For low wind speeds, the lowest flux measurement level may not be sufficiently close to the surface to estimate the surface fluxes. To assess potential flux errors, we assume that the 1-m values of the momentum flux are a reasonable approximation to the surface fluxes and examine the errors associated with use of 5-m fluxes. For the different methods of compositing the momentum flux and the different $\delta\theta$ classes in Figs. 6–7, the surface flux error using the composited 5-m fluxes is typically 5%–20%. The estimated errors for the heat flux are generally a little larger. Error estimates based on extrapolation of linear regression of the fluxes to the surface are somewhat larger than those based on the 1-m fluxes. The errors would be roughly twice the above values with use of 10-m fluxes.

The problem becomes more complex with microscale heterogeneity because the flux varies with height due to the increasing footprint with height. This issue is not an instrumental problem but rather a problem of representativeness and intent of the flux calculation. Defining the surface flux to be at the ground surface for use in the surface energy balance would correspond to a vanishing footprint. Ideally the site is homogeneous on the microscale where the increasing footprint with height close to the surface does not affect the flux. The microscale heterogeneity appears to be small at our sites with the possible exception of the SCP site. However, nearby flux stations in the network on the valley floor showed, on average, minimal spatial variations of the 1-m momentum flux. At higher levels on the FLOSSII, SCP and BPP towers, the flux footprint increases with height to the extent that it is capturing some of the rougher surface upwind, and this defines the transition layer studied in Sect. 5.

The material above did not consider deviations between the stress, wind and shear directions. Although such deviations can be large for individual events, vector averaging the stress and wind directions over the datasets revealed little systematic difference between the wind and stress directions except at the SCP site. At this site for low wind speeds, the systematic differences between the stress and wind directions based on composited wind and stress components reach 60° in the transition layer between the shallow down-valley flow at the surface and the overlying regional flow (not shown).

7 Conclusions

We examined turbulent flux measurements over four different surfaces where the surface roughness is greater upwind of the observational sites but disorganized. With low wind speeds, the vertical divergence of the momentum and heat flux is often large such that measurements at standard observational levels (2–10 m) are inadequate for estimation of the surface fluxes. For low wind speeds at the four sites, the mean surface-flux error using 5-m measurements was estimated to be 5%–20%. Such errors lead to miscalibration of similarity theory and contribute to errors in the surface energy budget.

With flow from complex rougher surfaces to smoother surfaces, the magnitudes of the downward momentum and heat fluxes close to the surface sometimes decreases rapidly with height in a shallow new boundary layer adjusting to the new surface. The new boundary layer is analogous to an internal boundary layer that develops with flow past a single sharp decrease of surface roughness. Above the new boundary layer, the flux magnitudes increase with height in a transition layer, reaching a maximum at the top of the transition layer as idealized in Fig. 5. The flux magnitudes then decrease with height in an overlying regional boundary layer. Such significant flux divergence (convergence) can occur even with disorganized weak surface heterogeneity. Over the two sites with more significant surface heterogeneity, the depth scale of the heat flux profile is smaller than that for momentum, suggesting that any analogy with internal boundary layers is incomplete, although the cause of this difference of depth scales was not isolated.

For the measurements of our study with low wind speeds, the magnitude of the downward momentum and heat fluxes close to the surface decrease rapidly with height in common shallow drainage flows and also in shallow polar Ekman layers over flat ice/snow surfaces (5-m depth, Grachev et al. (2005)) where the flow is relatively stationary and the surface roughness length is small. Elevated generation of turbulence and fluxes, often associated with a low-level jet, can also contribute to the increase of the flux magnitudes with height. With higher wind speeds, the vertical divergence of the flux close to the surface is generally less important in our study, except with flow over the gentle topography at the SCP site where lee-generated turbulence sometimes leads to a rapid increase of the flux magnitudes with height.

Because the behaviour of the flux divergence is site dependent, analysis of more datasets is required. In addition, long datasets are required to partition the analysis into different wind directions and into different regimes based on stability, non-stationarity, low-level jets and so forth. The flux divergence is more vulnerable to flux errors than the flux itself, discussed in Sect. 2.2. Although it is not obvious how the flux errors could explain the systematic height dependence of the flux, more investigation is required. To estimate surface fluxes, measurements are required close to the surface, preferably at 1 m or lower, provided that the flux loss due to path-length averaging is not important and the measurements are above the roughness sublayer. Smaller path lengths or supplemental instrumentation such as hot film anemometers would be potentially useful.

Acknowledgements We gratefully acknowledge the extensive comments of the reviewers that led to major improvements of the manuscript. Discussions with Ivana Stiperski significantly improved our perspective on the impact of sloped terrain on flux measurements. This project received support from Grant AGS-1614345 from the National Science Foundation. The Earth Observing Laboratory of the National Center for Atmospheric Research provided the measurements from the FLOSSII and SCP campaigns. We acknowledge the hard work by scientists and staff involved in collection of the SHEBA turbulence data, especially Christopher Fairall, Peter Guest, and the late Ed Andreas. The SHEBA data collection and analysis was supported by Grants OPP-97-01766 and OPP-00-84323 from the U. S. National Science Foundation. OP and AG were supported by funds from the National Oceanic and Atmospheric Administration/Earth System Research Laboratory/Physical Sciences Division during the preparation of this manuscript. Emily Andreas Moynihan prepared Fig. 5.

References

Acevedo O, Mahrt L (2010) Systematic vertical variation of mesoscale fluxes in the stable boundary layer. Boundary-Layer Meteorol 135:19–30

Acevedo O, Moraes O, Degrazia G, Fitzjarrald D, Manzi A, Campos J (2009) Is friction velocity the most appropriate scale for correcting nocturnal carbon dioxide fluxes? Agric For Meteorol 149:1–10

Acevedo O, Mahrt L, Puhales FS, Costa FD, Medeiros LE, Degrazia GA (2015) Contrasting structures between the decoupled and coupled states of the stable boundary layer. Q J R Meteor Soc 142:693–702

Balsley B, Frehlich RG, Jensen ML, Meillier Y (2006) High-resolution in situ profiling through the stable boundary layer: Examination of the SBL top in terms of minimum shear, maximum stratification, and turbulence decrease. J Atmos Sci 63:1291–1307

Banta RM, Pichugina YL, Brewer W (2006) Turbulent velocity-variance profiles in the stable boundary layer generated by a nocturnal low-level jet. J Atmos Sci 63:2700–2719

Basu S, Porté-Agel F, Foufoula-Georgiou E, Vinuesa JF, Pahlow M (2006) Revisiting the local scaling hypothesis in stably stratified atmospheric boundary-layer turbulence: an integration of field and laboratory measurements with large-eddy simulations. Boundary-Layer Meteorol 119:473–500

Bou-Zeid E, Parlange M, Meneveau C (2007) On the parameterization of surface roughness at regional scales. J Atmos Sci 64:216–227

Cardon SJ (2007) Obtaining eddy fluxes for a non-homogeneous environment using wavelet cospectra. Master's thesis, University of Wyoming

Conangla L, Cuxart J (2006) On the turbulence in the upper part of the low-level jet: An experimental and numerical study. Boundary-Layer Meteorol 118:379–400

Dellwik E, Jensen NO (2000) Internal equilibrium layer growth over forest. Theor Appl Climatol 66:173–184

Dellwik E, Bingöl F, Mann J (2013) Flow distortion at a dense forest edge. Q J R Meteor Soc 140:676–686

Garratt JR (1990) The internal boundary layer – A review. Boundary-Layer Meteorol 50:171–203

Garratt JR (1994) The Atmospheric Boundary Layer. Cambridge University Press, Cambridge, UK, 316 pp

Glendening JC, Lin CL (2002) Large eddy simulation of internal boundary layers created by changes in surface roughness. J Atmos Sci 59:1697–1711

Grachev A, Fairall C, Persson P, Andreas E, Guest P (2005) Stable boundary-layer scaling regimes: The SHEBA data. Boundary-Layer Meteorol 116:201–235

Grachev A, Andreas E, Fairall C, Guest P, Persson P (2013) The critical Richardson number and limits of applicability of local similarity theory in the stable boundary layer. Boundary-Layer Meteorol 147:51–82

Grachev A, Leo LS, Fernando HJS, Fairall CW, Creegan E, Blomquist B, Christman A, Hocut C (2018) Air-sea/land interaction in the coastal zone. Boundary-Layer Meteorol 167:181–210

Grisogono B, Oerlemans J (2001) Katabatic flow: Analytical solution for slowly varying eddy diffusivities. J Atmos Sci 58:3349–3354

Horst TW, Oncley SP (2006) Corrections to inertial-rage power spectra measured by CSAT3 and Solent sonic anemometers, 1. path-averaging errors. Boundary-Layer Meteorol 119:375–395

Horst TW, Semmer SR, Maclean G (2015) Correction of a non-orthogonal, three-component sonic anemometer for flow distortion by transducer shadowing. Boundary-Layer Meteorol 155:371–395

Irvine M, Gardiner B, Hill M (1997) The evolution of turbulence across a forest edge. Boundary-Layer Meteorol 84:467–496

Kallistratova MA, Kouznetsov RD (2012) Low-level jets in the Moscow region in summer and winter observed with a sodar network. Boundary-Layer Meteorol 143:159–175

Liu H (2001) New equations for sonic temperature variance and buoyancy heat flux with an omindirectional sonic anemometer. Boundary-Layer Meteorol 100:459–468

Mahrt L (2017) Lee mixing and nocturnal structure over gentle terrain. J Atmos Sci 74:1989–1999

Mahrt L, Thomas CK (2016) Surface stress with non-stationary weak winds and stable stratification. Boundary-Layer Meteorol 159:3–21

Mahrt L, Vickers D (2002) Contrasting vertical structures of nocturnal boundary layers. Boundary-Layer Meteorol 105:351–363

Mahrt L, Vickers D (2005) Boundary-layer adjustment over small-scale changes of surface heat flux. Boundary-Layer Meteorol 116:313–330

Mahrt L, Vickers D (2006) Extremely weak mixing in stable conditions. Boundary-Layer Meteorol 119:19–39

Mahrt L, Sun J, Oncley SP, Horst TW (2014) Transient cold air drainage down a shallow valley. J Atmos Sci 71:2534–2544

Moore CJ (1986) Frequency response corrections for eddy correlation methods. Boundary-Layer Meteorol 37:17–35

Morse AP, Gardiner BA, Marshall BJ (2002) Mechanisms controlling turbulence development across a forrest edge. Boundary-Layer Meteorol 103:227–251

Mortarini L, Cava D, Giostra U, Acevedo O, Nogueira Martins LG, Soares de Oliveira PE, Anfossi D (2017) Observations of submeso motions and intermittent turbulent mixing across a low level jet with a 132-m tower. Q J R Meteor Soc 144:172–183

Nadeau DF, Pardyjak ER, Higgins CW, Huvald H, Parlange MB (2013) Flow during the evening transition over steep alpine slopes. Q J R Meteor Soc 139:607–624

Nappo C (1991) Sporadic breakdown of stability in the PBL over simple and complex terrain. Boundary-Layer Meteorol 54:69–87

Pahlow M, Parlange M, Porté-Agel F (2001) Richardson number statistics in the seasonal thermocline. Boundary-Layer Meteorol 99:225–248

Persson P, Vihma T (2017) The atmosphere over sea ice. In: Thomas DN (ed) Sea Ice, Wiley-Blackwell, London, chap 6, pp 160–196

Persson P, Fairall CW, Andreas EL, Guest PS, Perovich DK (2002) Measurements near the atmospheric surface flux group tower at SHEBA: near-surface conditions and surface energy budget. J Geophys Res 107, DOI 10.1029/2000JC000705

Persson POG, Shupe M, Perovich D, Solomon A (2017) Linking atmospheric synoptic transport, cloud phase, surface energy fluxes, and sea-ice growth: Observations of midwinter sheba conditions. Clim Dyn 49:1341–1364

Pöette C, Gardiner B, Dupont S, Harman I, Böhm M, Finnigan J, Hughes D, Brunet Y (2017) The impact of landscape fragmentation of atmospheric flow: A wind-tunnel study. Boundary-Layer Meteorol 163:393–421

Poulos G, Burns S (2003) An evaluation of bulk Ri-based surface layer flux formulations for stable and very stable conditions with intermittent turbulence. J Atmos Sci 60:2523–2537

Schmid H, Bünzli D (1995) The influence of surface texture on the effective roughness length. Q J R Meteor Soc 121A:1–21

Skyllingstad ED, Samelson RM, Mahrt L, Barbour P (2005) A numerical modeling study of warm offshore flow over cool water. Mon Weather Rev 133:345–361

Smedman AS (1988) Observations of a multi-level turbulence structure in a very stable atmospheric boundary layer. Boundary-Layer Meteorol 44:231–253

Stiperski I, Rotach MW (2016) On the measurement of turbulence over complex mountainous terrain. Boundary-Layer Meteorol 159

Sun J, Mahrt L, Banta RM, Pichugina YL (2012) Turbulence regimes and turbulence intermittency in the stable boundary layer during CASES-99. J Atmos Sci 69:338–351

Sun J, Lenschow D, Mahrt L, Nappo C (2013) The relationships among wind, horizontal pressure gradient and turbulent momentum transport during CASES99. J Atmos Sci 70:3397–3414

Thomas CK, Kennedy A, Selker J, Moretti A, Schroth M, Smoot A, Tufillaro N (2012) High-resolution fibre-optic temperature sensing: A new tool to study the two-dimensional structure of atmospheric surface-layer flow. Boundary-Layer Meteorol 142:177–192

Van de Wiel BJH, Moene AF, Steeneveld GJ, Baas P, Bosveld FC, Holtslag AAM (2010) A conceptual view on inertial oscillations and nocturnal low-level jets. J Atmos Sci 67:2679–2689

Wilczak J, Oncley S, Sage SA (2001) Sonic anemometer tilt correction algorithms. Boundary-Layer Meteorol 99:127–150

Williams A, Chambers S, Griffiths S (2013) Bulk mixing and decoupling of the stable nocturnal boundary layer characterized using a ubiquitous natural tracer. Boundary-Layer Meteorol 149:381–402

Zeeman MJ, Selker JS, Thomas C (2015) Near-surface motion in the nocturnal, stable boundary layer observed with fibre-optic distributed temperature sensing. Boundary-Layer Meteorol 154:189–205